# Synthesis of Bandgap-Controlled Semiconducting Single-Walled Carbon Nanotubes

**Wooseok Song,[†] Cheolho Jeon,[†] Yoo Seok Kim,[†] Young Taek Kwon,[†] Dae Sung Jung,[†] Sung Won Jang,[†] Won Chel Choi,[†] Jin Sung Park,[‡] Riichiro Saito,[‡] and Chong-Yun Park[†,§,*]**

[†]BK21 Physics Research Division and Center for Nanotubes and Nanostructured Composites (CNNC), Sungkyunkwan University, Suwon 440-746, Republic of Korea, , [‡]Department of Physics, Tohoku University, Sendai, 980-8578, Japan, , and [§]Department of Energy Science, Sungkyunkwan University, Suwon 440-746, Republic of Korea

**ABSTRACT** Bandgap-controlled semiconducting single-walled carbon nanotubes (s-SWNTs) were synthesized using a uniquely designed catalytic layer (Al$_2$O$_3$/Fe/Al$_2$O$_3$) and conventional thermal chemical vapor deposition. Homogeneously sized Fe catalytic nanoparticles were prepared on the Al$_2$O$_3$ layer and their sizes were controlled by simply modulating the annealing time *via* heat-driven diffusion and subsequent evaporation of Fe at 800 °C. Transmission electron microscopy and Raman spectroscopy revealed that the synthesized SWNTs diameter was manipulated from 1.4 to 0.8 nm with an extremely narrow diameter distribution below 0.1 nm as the annealing time is increased. As a result, the bandgap of semiconducting SWNTs was successfully controlled, ranging from 0.53 to 0.83 eV, with a sufficiently narrow energy distribution, which can be applied to field-effect transistors based on SWNTs.

S emiconducting single-walled carbon nanotube (s-SWNT) has a great potential for applications in future field effect transistors (FETs) owing to its excellent electrical properties.[1−8] To realize FETs based on s-SWNTs, the s-SWNTs should have a fixed energy bandgap in order to obtain the same responses from the FETs as a function of the gate voltage. Demonstrating the importance of bandgap control, it was recently reported that the bandgap was the main parameter responsible for the on-current of the FETs and could vary by up to 3 orders of magnitude.[9] Accordingly, the main pursuit in the synthesis of s-SWNTs has been to control the diameter so as to attain the desired energy bandgap which is inversely proportional to the tube diameter.[1] There have been various approaches to synthesize diameter-controlled SWNTs by preparation of homogeneously sized catalysts, because the SWNT diameter highly depends on the catalytic nanoparticle size.[10] To obtain homogeneously sized catalysts, one should consider catalytic metal species and preparation methods for

restricting their size, such as using a template of anodic aluminum oxide[11] and handling process of organic molecules.[12] Although the species of catalytic nanoparticle have been extended from the common iron-group metals (Fe, Co, Ni) to noble metals and Cu,[13,14] the iron-group metals have been chosen for controlling nanoparticle size precisely. Several groups have reported that some (*n,m*) nanotubes were selectively synthesized with CoMoCAT by the chemical vapor deposition (CVD) method, but the diameter control was not achieved.[15−17] Using laser furnace technique, the central diameter was changed by modulating the furnace temperature with several catalysts, but the diameter distributions were not sufficiently narrow (0.2−0.4 nm).[18] Fe catalysts have also been adopted for diameter control using identical molecular nanoclusters containing Fe[19−21] and Fe nanoparticles incorporated with Al oxide.[22,23] These methods, however, still show wide tube diameter distributions (0.2−3.0 nm) due to the broad size distribution of Fe nanoparticles. Therefore, a new method for catalyst preparation is required to synthesize s-SWNTs with desired bandgaps.

In this study, we report on the successful synthesis of bandgap-controlled s-SWNTs using a uniquely designed catalytic layer and conventional thermal CVD (TCVD) system through precise control of the diameter having an extremely narrow distribution. The catalytic layer was fabricated by introducing a Fe catalyst between the two Al$_2$O$_3$ layers. Homogeneously sized Fe nanoparticles were prepared on the Al$_2$O$_3$ layer, and their sizes were controlled by modulating the annealing time at 800 °C *via* heat-driven diffusion and subsequent
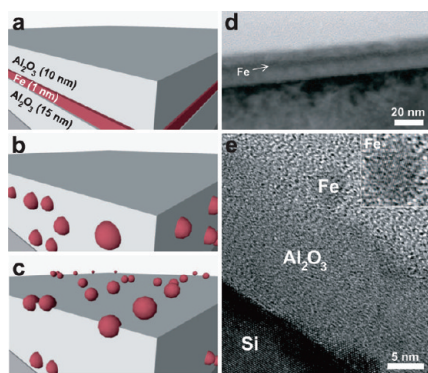
Figure 1. Schematic diagrams and TEM images of the heat-driven Fe diffusion phenomenon: (a) designed catalytic layer of $Al_2O_3$/Fe/$Al_2O_3$ on a Si(001) substrate; (b, c) schematic diagrams for the heat-driven diffusion of Fe nanoparticles during the annealing process; (d) cross-sectional TEM image of as-deposited catalytic layer consisting of $Al_2O_3$ (10 nm)/Fe (1 nm)/$Al_2O_3$ (15 nm)/Si(001) substrate; (e) cross-sectional TEM image of the catalytic layer after annealing at 800 °C for 10 min shows the Fe nanoparticles of ~3 nm in diameter on the $Al_2O_3$ layer. The inset reveals a crystalline structure of Fe nanoparticle.

evaporation of Fe. Consequently, by adjusting the pre-annealing time, the SWNTs diameter and fine distribution were successfully controlled on a scale of a few Å and below 1 Å, respectively. These precise control techniques allowed for the bandgap manipulation of s-SWNTs from 0.53 to 0.83 eV, which was confirmed by direct comparison of Raman spectra and an extended tight binding (ETB) Kataura plot.[24]

## RESULTS AND DISCUSSION

A uniquely designed catalytic layer structure and annealing process were employed to control the size of catalytic Fe nanoparticles. Figure 1 shows (a—c) schematic diagrams and (d, e) high-resolution transmission electron microscopy (HR-TEM) images of the catalytic layer used in this experiment. The layer was designed and fabricated by placing the 1 nm thick Fe catalyst between the two $Al_2O_3$ layers of 10 nm (top) and 15 nm (bottom), as shown in panels a and d. An annealing process was employed to induce heat-driven Fe diffusion toward the surface and to form size-controlled Fe catalytic nanoparticles on the $Al_2O_3$ layer, as shown in panels b and c. The phenomenon of heat-driven Fe diffusion across the $Al_2O_3$ layers can be described by the temperature-dependent impurity diffusion coefficient (diffusivity),

$$D = D_0 \exp\left(\frac{-E_A}{k_B T}\right) \qquad (1)$$

where $D_0$ is the temperature-independent pre-exponential ($m^2$/s) and $E_A$ is the activation energy for diffusion (J/mol).[25–27] The corresponding vertical diffusion length ($L_{VD}$) is determined by the diffusivity ($D$) and the diffusion time ($t$).[27]

$$L_{VD} = 4(Dt)^{1/2} \qquad (2)$$

This indicates that heat-driven Fe diffusion can be controlled by the annealing temperature and time. The success of the diffusion was confirmed by TEM observations of the catalytic layer after annealing at 800 °C for 10 min. The TEM images clearly show that after annealing, the layerlike Fe catalyst (denoted by an arrow) in Figure 1d disappears and Fe nanoparticles appear at the top of the $Al_2O_3$ layer, as displayed in Figure 1e. The inset shows that the Fe nanoparticles are well-crystallized with diameters of ~3 nm. Each chemical component was identified by energy dispersive X-ray spectroscopy (not shown). After numerous experiments under different conditions, the optimized diffusion conditions, that is, an annealing temperature of 800 °C and an $Al_2O_3$ overlayer thickness of 10 nm, were carefully adopted.

X-ray photoelectron spectroscopy (XPS) was used for a detailed examination of the heat-driven Fe diffusion phenomenon, as shown in Figure 2. The catalytic layer, $Al_2O_3$ (10 nm)/Fe (1 nm)/$Al_2O_3$ (15 nm), was deposited on a Si(001) substrate by DC magnetron sputtering, as shown in Figure 1d. The Fe 2p core level spectra were obtained from the $Al_2O_3$ (10 nm)/Fe (1 nm)/$Al_2O_3$ (15 nm)/Si substrate using a VG Microtech ESCA 2000 with a monochromatic Al Kα radiation (1486.6 eV). Figure 2a shows the evolution of the Fe 2p spectra according to the annealing time (0—60 min) at 800 °C. The underlying Fe layer exhibits negligible intensity in the spectrum prior to annealing. As the annealing time is increased, a spectral shape is observed with binding energies of 707 and 720 eV corresponding to the Fe $2p_{3/2}$ and $2p_{1/2}$ core levels, respectively.[28] This shows that the Fe nanoparticles are pure metals suitable for use as an active catalyst for carbon nanotube (CNT) synthesis. The intensity of the Fe 2p spectra is plotted as a function of annealing time in Figure 2b. After annealing at 800 °C for 5 min (region I), the intensity increased to 250% of its initial value. On the other hand, there is an abrupt decrease between 5 and 10 min, followed by a gradual decrease up to 60 min (region II). In region I, the sudden intensity increase during 1 min can be explained by the formation of Fe nanoparticles on the $Al_2O_3$ layer as a result of heat-driven Fe diffusion. It is expected from eq 2 that only 30 s are necessary to diffuse the Fe catalyst across the 10 nm $Al_2O_3$ layer, where $D$ is estimated as $5 \times 10^{-18}$ $cm^2$/sec.[27]

Since the decrease in intensity in region II cannot be completely understood by heat-driven diffusion, the size of the Fe nanoparticles was observed by HR-TEM (JEOL, JEM2100F). Figure 2c—e show the Fe nanoparticles on the $Al_2O_3$ layer after annealing at 800 °C for 1, 10, and 30 min, respectively. The average size of the Fe nanoparticles, which are uniform, clearly decreases from (c) ~3 nm to (d) ~2.2 nm to (e) ~1.7 nm as the annealing time increases. This would be explained by the evaporation of Fe even though the temperature is lower than that of bulk Fe because nanoparticles have
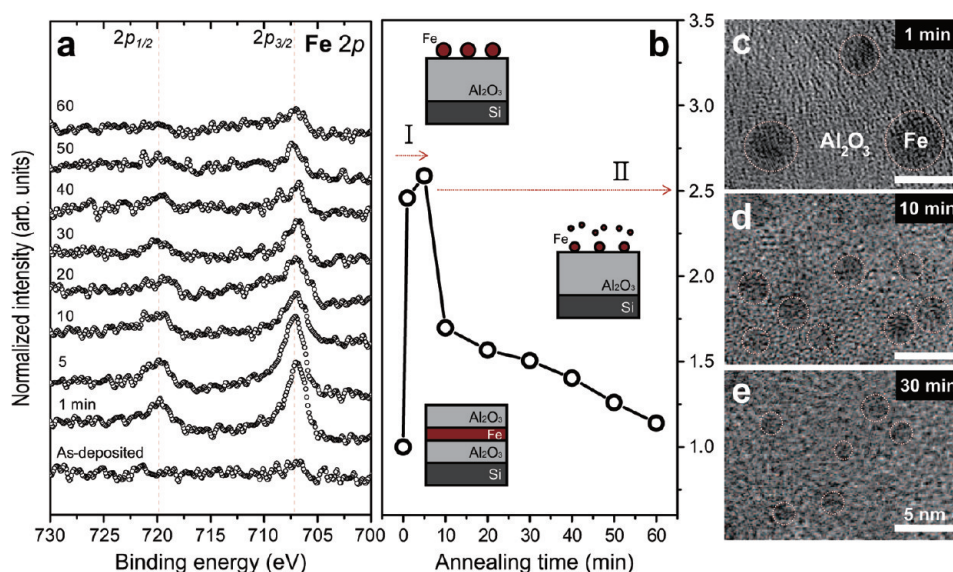
Figure 2. (a) Evolution of the Fe 2p core level spectra corresponding to the annealing time. (b) Plot of the Fe 2p intensity as a function of annealing time. The insets show schematic diagrams of the diffusion and subsequent evaporation phenomena of the Fe nanoparticles with an increase in annealing time. HR-TEM images (top view) of Fe nanoparticles on the $Al_2O_3$ layer after annealing for (c) 1 min, (d) 10 min, and (e) 30 min. Red circles indicate the Fe nanoparticles, and the scale bars are 5 nm.

a lower onset temperature of melting and evaporation.[29,30] Jeong *et al*. reported that Co nanoparticles were thermally evaporated by annealing at 1000 °C in Ar ambient of 500 Torr.[31] The evaporation rate of Fe (∼0.043 nm/min) in this experiment is two times higher than that of Co (∼0.023 nm/min) in ref 31. This discrepancy can be understood by two orders lower ambient pressure in this experiment promoting the evaporation of Fe. On the other hand, aggregation of Fe nanoparticles was not observed during annealing at 800 °C. This will be responsible for an appropriate roughness of the $Al_2O_3$ overlayer that acts as a surface diffusion barrier of Fe.[32,33] Since the annealing condition produced size-controlled Fe nanoparticles without aggregation, we adopted heat-driven diffusion and

subsequent evaporation process (HDSEP) to synthesize SWNTs having different diameters for each condition.

CNTs were synthesized using a TCVD system on the catalytic layer prepared by HDSEP. Note that the obtained CNTs are denoted by H0, H10, and H30 corresponding to HDSEP time of 0, 10, and 30 min at 800 °C, respectively. The structural characteristics of the synthesized CNTs were investigated by field-emission scanning electron microscopy (FE-SEM, JEOL, JSM6700F) and HR-TEM. Figure 3 panels a, b, and c show FE-SEM images of H0, H10, and H30, respectively. The images reveal that the CNTs were synthesized as a well-defined network configuration laterally on the substrates regardless of the HDSEP time. This confirms that heat-driven Fe diffusion occurred toward the $Al_2O_3$ surface
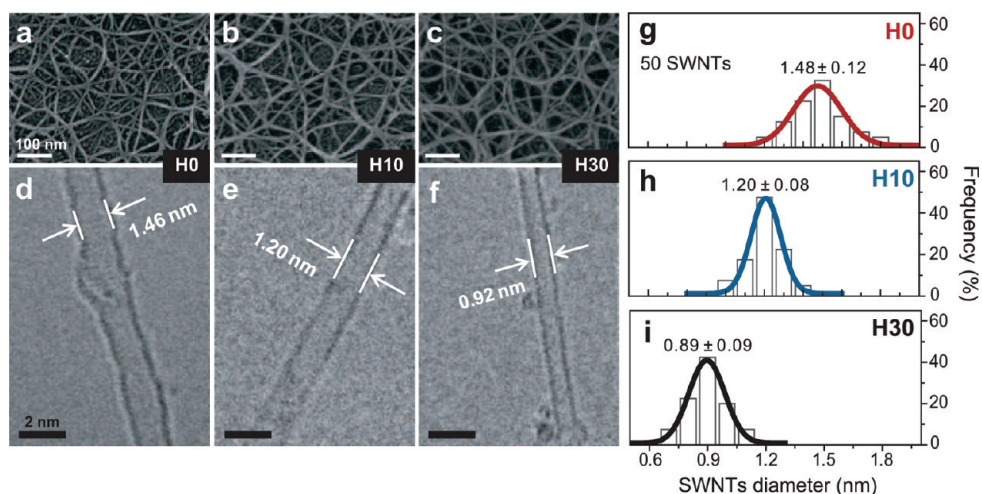


Figure 3. (a−c) FE-SEM images show that the SWNTs are synthesized as a well-defined network configuration laterally on the substrates regardless of the HDSEP time. (d−f) HR-TEM images display the changes in the SWNT diameter from 1.46 to 0.92 nm as the HDSEP time is increased. The histograms show the diameter distributions for (g) H0, (h) H10, and (i) H30. The scale bars of the FE-SEM and HR-TEM images are 100 and 2 nm, respectively.

as shown in Figure 2c–e because Al is unsuitable as a catalyst for CNT synthesis. In addition, the synthesis of H0 implies that Fe nanoparticles as nucleation sites for CNTs were formed on the $Al_2O_3$ layer *via* fast heat-driven Fe diffusion as confirmed in Figure 2c. HR-TEM images reveal that H0, H10, and H30, shown in Figure 3 panels d, e, and f, respectively, have only one layer and are of a high quality without amorphous carbon formation. As expected, the SWNTs exhibit different diameters corresponding to the annealing time. Figure 3 panels g–i show the diameter distributions obtained from an analysis of the HR-TEM images of each sample. The mean diameters of H0, H10, and H30 are estimated to be 1.48, 1.20, and 0.89 nm with standard deviations of 0.12, 0.08, and 0.09 nm, respectively. This unambiguously shows that the SWNTs diameter is decreased corresponding to the size of Fe nanoparticles as HDSEP time is increased.

The radial breathing modes (RBMs) of the resonant Raman spectra, which were obtained using a Renishaw 1000 micro-Raman spectrometer with an excitation wavelength of 514 nm, were investigated to confirm the reproducibility of the SWNTs in terms of the diameter control. The spectra were recorded from various samples under each condition, as shown in Figure 4. The role of the $Al_2O_3$ overlayer in controlling the SWNT diameter was the first factor to be investigated. Figure 4a shows that the synthesized CNTs without the $Al_2O_3$ overlayer have a wide diameter distribution. In contrast, the samples with the $Al_2O_3$ overlayer treated by means of HDSEP exhibit extremely narrow and homogeneous diameter distributions, as shown in Figure 4b–d. The diameters were calculated according to the relationship between the RBM frequency and SWNTs diameter.[34] The diameter distributions for H0, H10, and H30 are 1.42 ± 0.03, 1.28 ± 0.02, and 0.88 ± 0.02 nm, respectively, which are in good agreement with the TEM results in Figure 3. This indicates that the diameter of the SWNTs and its fine distribution can be controlled on a scale of a few Å and below 1 Å, respectively, by varying only the HDSEP time. We note that the SWNTs diameter synthesized after the HDSEP time of 20 min was not well-controlled and SWNTs were not observed after the HDSEP time of 40 min.

The electrical properties of the synthesized SWNTs were examined by assigning their structural (n,m) indices. Raman spectra were obtained using two excitation wavelengths, 514 and 633 nm, in order to extract more information of the SWNT through the different resonance Raman scattering. Figure 5 exhibits the overviews (a, b, c) and RBMs (d, e, f) of the Raman spectra for H0, H10, and H30, respectively. All the spectra were normalized to G-band at 1591 cm$^{-1}$. The extremely weak defect feature (D-band) at 1340 cm$^{-1}$ indicates that highly crystalline SWNTs were synthesized. The G-bands of H0 and H10 at 633 nm as well as H30 at 514
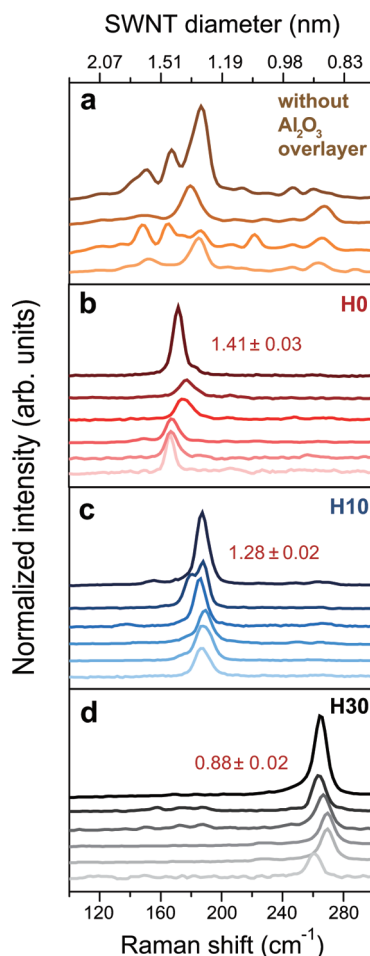


**Figure 4.** RBM analysis from the Raman spectra with an excitation wavelength of 514 nm of (a) the synthesized SWNTs without the $Al_2O_3$ overlayer, (b) H0, (c) H10, and (d) H30. Each spectrum was taken from different samples.

nm exhibit metallic features, which are determined by the presence of a Breit–Wigner–Fano line shape,[35,36] as shown in Figure 5a–c. The other Raman spectra exhibit semiconducting features of the G-band with the two excitation wavelengths. The electronic structure was also determined using the RBM spectra and the ETB Kataura plot. The $E_{11}^M$ energy transition between the two van Hove singularities in the density of states was observed at excitation wavelengths of 514 nm for H0 and H10 as well as 633 nm for H30, as shown in Figure 5d–f. On the other hand, the s-SWNTs show different energy transitions, such as $E_{44}^S$ for H0, $E_{33}^S$ for H10, and $E_{22}^S$ for H30. The assignment of (n,m) indices for the SWNTs was carried out by fitting the RBM components with a Lorentzian function. The fitted components were labeled with (n,m) indices using the ETB Kataura plot. The assigned indices of the metallic-SWNTs (m-SWNTs) are (9,9) and (14,2) for H0, (11,5) and (12,6) for H10, and (8,5) and (12,0) for H30. The assigned indices of the s-SWNTs are (14,6) for H0, (16,2) and (13,5) for H10, and (11,1), (8,4), and (10,0) for H30. The indices were chosen within the resonance window of 1.83–2.01 and 2.31–2.45 eV
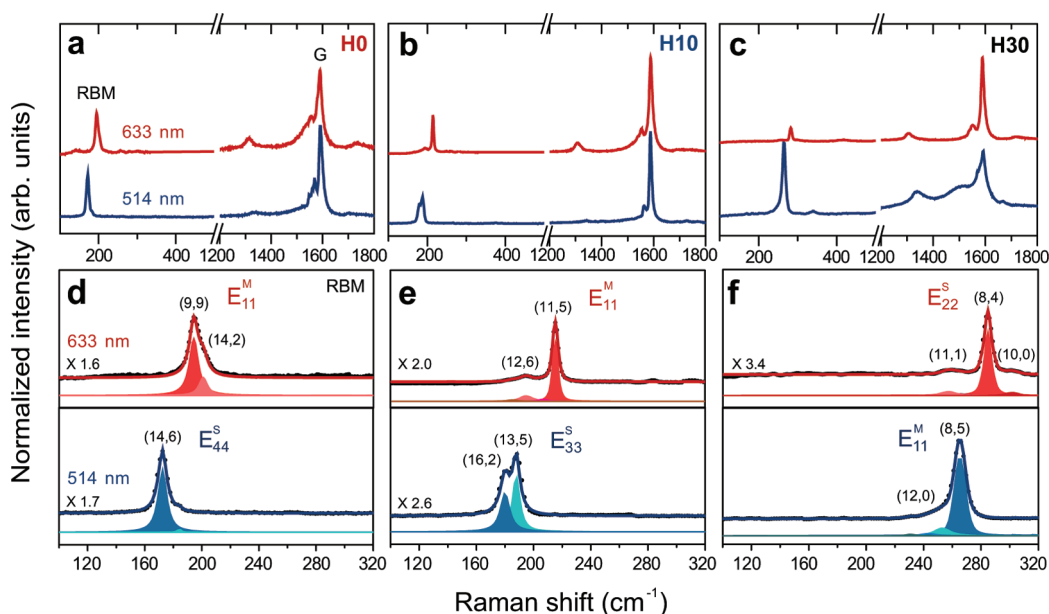
**Figure 5. Raman spectra with 633 (red) and 514 nm (blue) excitation wavelengths. (a, b, c) Overview and (d, e, f) RBM spectra of H0, H10, and H30, respectively. The structural (n,m) indices and transition energies were derived from the ETB Kataura plot.**

for excitation energies of 1.96 eV (633 nm) and 2.41 eV (514 nm), respectively.[37]

To examine whether the bandgap energy and its energy distribution had been sufficiently controlled to apply to FETs, the diameter distributions of the s-SWNTs in H0 (red), H10 (blue), and H30 (gray) were projected on the Kataura plot showing the $E_{11}^S$ transition energy (bandgap energy) as a function of SWNT diameter, as can be seen in Figure 6. The diameter distributions were
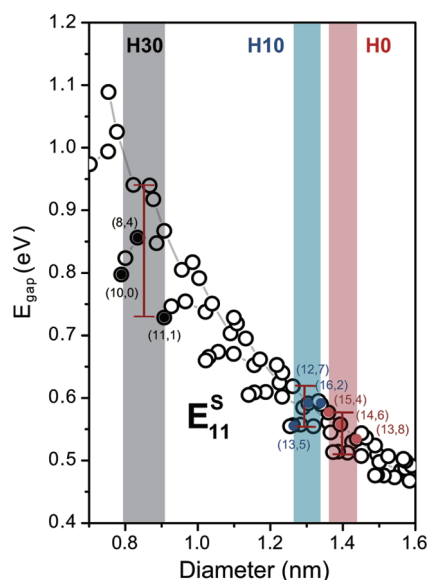


**Figure 6. The diameter distributions of the s-SWNTs in H0 (red), H10 (blue), and H30 (gray) are projected on $E_{11}^S$ transition energy of the Kataura plot as a function of SWNT diameter calculated from the ETB method. The closed circles indicate the (n,m) SWNTs derived from RBM analysis of the Raman spectra in Figures 4 and 5. The red bars indicate the bandgap energy distributions corresponding to the diameter distributions.**

determined by the extracted (n,m) indices from more than 20 samples for each condition with the two excitation energies. Remarkably, each sample has only three types of s-SWNTs: (13,8), (14,6), and (15,4) for H0, (16,2), (12,7), and (13,5) for H10, and (11,1), (8,4), and (10,0) for H30. The red bar indicate the bandgap energy distributions of H0 (0.53 ± 0.03 eV), H10 (0.59 ± 0.03 eV), and H30 (0.83 ± 0.1 eV) corresponding to the diameter distributions. We can conclude that direct synthesis of bandgap-controlled SWNTs has been successfully achieved by TCVD using the uniquely designed catalytic layer and by adjusting the HDSEP time. Even though we did not accomplish the preferential growth of s-SWNTs *versus* m-SWNTs, the bandgap-controlled s-SWNTs can be obtained after burning out m-SWNTs.[38] H0 and H10 can be used in FETs based on SWNTs because their bandgaps and narrow distributions have suitable values[9] in comparison with the previous results,[16,17] where smaller diameter SWNTs (0.6 − 1.1 nm) were synthesized without a diameter control. H30 will be also useful for applications requiring wider bandgap energies similar to silicon.

## CONCLUSION

We report the successful synthesis of bandgap-controlled s-SWNTs using a uniquely designed catalytic layer and TCVD system. TEM and XPS results revealed that homogeneously sized Fe nanoparticles were prepared on the $Al_2O_3$ layer *via* heat-driven Fe diffusion and that their size decreased uniformly *via* subsequent evaporation of Fe as the annealing time increased. As a result, the SWNTs diameter was manipulated from 1.4 to 0.8 nm with extremely narrow diameter distributions below 0.1 nm. Since the SWNTs exhibited highly selective structural

(n,m) indices for each condition, the s-SWNTs had different energy bandgaps ranging from 0.53 to 0.83 eV. We suggest that this result provides a simple way for direct synthesis of bandgap-controlled s-SWNTs *via* precise engineering of their diameters, which will be in demand for future applications.

## METHODS

The catalytic layer, Al$_2$O$_3$ (10 nm)/Fe (1 nm)/Al$_2$O$_3$ (15 nm), was prepared on a Si(001) substrate by DC magnetron sputtering and subsequent oxidation for each Al layer in air at room temperature for 3 h. The chemical components of Al overlayer were observed by XPS. It was oxidized to Al$_2$O$_3$ form in part (70%) during the oxidation in air and was fully oxidized during increasing temperature up to 600 °C to carry out HDSEP (not shown here). The sample was loaded into a TCVD system, followed by HDSEP at 800 °C in Ar (800 sccm) and H$_2$ (100 sccm) flows for 0, 10, and 30 min. Acetylene (C$_2$H$_2$) as a carbon feedstock with the Ar/H$_2$ mixture was then introduced into the TCVD system in order to synthesize the CNTs. The C$_2$H$_2$ was turned off after 10 min after which the TCVD reactor was cooled under the Ar/H$_2$ environment.

## REFERENCES AND NOTES

1. Saito, R.; Fujita, M.; Dresselhaus, G.; Dresselhaus, M. S. Electronic Structure of Chiral Graphene Tubules. *Appl. Phys. Lett.* **1992**, *60*, 2204.
2. Javey, J., A.; Guo; Wang, Q.; Lundstrom, M.; Dai, H. Ballistic Carbon Nanotube Field- Effect Transistors. *Nature* **2003**, *424*, 654–657.
3. Tans, S. J.; Verschueren, A. R. M.; Dekker, C. Room-Temperature Transistor Based on a Single Carbon Nanotube. *Nature* **1998**, *393*, 49–52.
4. Dulrkop, T.; Getty, S. A.; Cobas, E.; Fuhrer, M. S. Extraordinary Mobility in Semiconducting Carbon Nanotubes. *Nano Lett.* **2004**, *4*, 35–39.
5. Wind, S. J.; Appenzeller, J.; Avouris, P. Lateral Scaling in Carbon-Nanotube Field-Effect Transistors. *Phys. Rev. Lett.* **2003**, *91*, 106102.
6. Javey, A.; Guo, J.; paulsson, m.; Wang, Q.; Mann, D.; Lundstrom, M.; Dai, H. High-Field Quasiballistic Transport in Short Carbon Nanotubes. *Phys. Rev. Lett.* **2004**, *92*, 106804.
7. Martel, R.; Schmidt, T.; Shea, H. R.; Hertel, T.; Avouris, P. Single- and Multi-Wall Carbon Nanotube Field-Effect Transistors. *Appl. Phys. Lett.* **1998**, *73*, 2447.
8. Byon, H. R.; Choi, H. C. Network Single-Walled Carbon Nanotube-Field Effect Transistors (SWNT-FETs) with Increased Schottky Contact Area for Highly Sensitive Biosensor Applications. *J. Am. Chem. Soc.* **2006**, *128*, 2188.
9. Chen, Z.; Appenzeller, J.; Knoch, J.; Lin, Y.; Avouris, P. The Role of Metal−Nanotube Contact in the Performance of Carbon Nanotube Field-Effect Transistors. *Nano Lett.* **2005**, *5*, 1497–1502.
10. Zhao, B.; Futaba, D. N.; Yasuda, S.; Akoshima, M.; Yamada, T.; Hata, K. Exploring Advantages of Diverse Carbon Nanotube Forests with Tailored Structures Synthesized by Supergrowth from Engineered Catalysts. *ACS Nano* **2009**, *3*, 108–114.
11. Yuan, Z.; Huang, H.; Liu, L.; Fan, S. Controlled Growth of Carbon Nanotubes in Diameter and Shape Using Template-Synthesis Method. *Chem. Phys. Lett.* **2001**, *345*, 39–43.
12. Inoue, T.; Gunjishima, I.; Okamoto, A. Synthesis of Diameter-Controlled Carbon Nanotubes Using Centrifugally Classified Nanoparticle Catalysts. *Carbon* **2007**, *45*, 2164–2170.
13. Takagi, D.; Homma, Y.; Hibino, H.; Suzuki, S.; Kobayashi, Y. Single-Walled Carbon Nanotube Growth from Highly Activated Metal Nanoparticles. *Nano Lett.* **2006**, *6*, 2642–2645.
14. Zhou, W.; Ding, J., L. Liu Role of Catalysts in the Surface Synthesis of Single-Walled Carbon Nanotubes. *Nano Res.* **2009**, *2*, 593–598.
15. Kitiyanan, B.; Alvarez, W. E.; Harwell, J. H.; Resasco, D. E. Controlled Production of Single-Walled Carbon Nanotubes by Catalytic Decomposition of CO on Bimetallic Co−Mo Catalysts. *Chem. Phys. Lett.* **2000**, *317*, 497–503.
16. Bachilo, S. M.; Balzano, L.; Herrera, J. E.; Pompeo, F.; Resasco, D. E.; Weisman, R. B. Narrow (n,m)-Distribution of Single-Walled Carbon Nanotubes Grown Using a Solid Supported Catalyst. *J. Am. Chem. Soc.* **2003**, *125*, 11186–11187.
17. Wang, B.; Patrick, P.; Wei, L.; Li, L.-J.; Yang, Y.; Chen, Y. (n,m) Selectivity of Single-Walled Carbon Nanotubes by Different Carbon Precursors on Co−Mo Catalysts. *J. Am. Chem. Soc.* **2007**, *129*, 9014–9019.
18. Kataura, H.; Kumazawa, Y.; Maniwa, Y.; Ohtsuka, Y.; Sen, R.; Suzuki, S.; Achiba, Y. Diameter Control of Single-Walled Carbon Nanotubes. *Carbon* **2000**, *38*, 1691–1697.
19. Jeong, G.; Yamazaki, A.; Suzuki, S.; Kobayashi, Y.; Homma, Y. Behavior of Catalytic Nanoparticles during Chemical Vapor Deposition for Carbon Nanotube Growth. *Chem. Phys. Lett.* **2006**, *422*, 83–88.
20. Li, Y.; Kim, W.; Zhang, Y.; Rolandi, M.; Wang, D.; Dai, H. Growth of Single-Walled Carbon Nanotubes from Discrete Catalytic Nanoparticles of Various Sizes. *J. Phys. Chem. B.* **2001**, *105*, 11424–11431.
21. Liu, Q.; Ren, W.; Chen, Z.-G.; Wang, D.-W.; Liu, B.; Yu, B.; Li, F.; Cong, H.; Cheng, H.- M. Diameter-Selective Growth of Single-Walled Carbon Nanotubes with High Quality by Floating Catalyst Method. *ACS Nano* **2008**, *2*, 1722–1728.
22. Zhong, G.; Iwasaki, T.; Robertson, J.; Kawarada, H. Growth Kinetics of 0.5 cm Vertically Aligned Single-Walled Carbon Nanotubes. *J. Phys. Chem. B.* **2007**, *111*, 1907–1910.
23. Lacerda, R. G.; Teo, K. B. K.; Teh, A. S.; Yang, M. H.; Dalal, S.; Jefferson, D. A. ; Durrell, J. H. ; Rupesinghe, N. L.; Roy, D.; Amaratunga, G. A. J.; *et al.* Thin-Film Metal Catalyst for the Production of Multi-Wall and Single-Wall Carbon Nanotubes. *J. Appl. Phys.* **2004**, *96*, 4456–4462.
24. Samsonidze, G. G.; Saito, R.; Kobayashi, N.; Gruneis, A.; Jiang, J.; Jorio, A.; Chou, S. G.; Dresselhaus, G.; Dresselhaus, M. S. Family Behavior of the Optical Transition Energies in Single-Wall Carbon Nanotubes of Smaller Diameters. *Appl. Phys. Lett.* **2004**, *85*, 5703–5705.
25. Javey, A.; Dai, H. Regular Arrays of 2 nm Metal Nanoparticles for Deterministic Synthesis of Nanomaterials. *J. Am. Chem. Soc.* **2005**, *127*, 11942–11943.
26. Nickel, N. H. Hydrogen Migration in Single Crystal and Polycrystalline Zinc Oxide. *Phys. Rev. B* **2006**, *73*, 195204.
27. Lenoble, O.; Bobo, J. F.; Hennet, L.; Fischer, H.; Bauer, P.; Piecuch, M. Structure, Magentism, and Thermal Stability of Fe-Al$_2$O$_3$ Multilayers. *Thin Solid Films* **1996**, *275*, 64–68.
28. Moulder, J. F.; Stickle, W. F.; Sobol, P. E.; Bomben, K. D. *Handbook of X-ray Photoelectron Spectroscopy*; Physical Electronics, Inc.: Chanhassen, MN, 1995.
29. Nanda, K. K.; Maisels, A.; Kruis, F. E.; Fissan, H.; Stappert, S. Higher Surface Energy of Free Nanoparticles. *Phys. Rev. Lett.* **2003**, *91*, 106102.
30. Ding, F.; Rosén, A.; Bolton, K. Size Dependence of the Coalescence and Melting of Iron Clusters: A Molecular-Dynamics Study. *Phys. Rev. B* **2004**, *70*, 075416.
31. Jeong, G.-H.; Suzuki, S.; Kobayashi, Y.; Yamazaki, Y.; Yoshimura, H.; Homma, Y. Size Control of Catalytic Nanoparticles by Thermal Treatment and Its Application

to Diameter Control of Single-Walled Carbon Nanotubes. *Appl. Phys. Lett.* **2007**, *90*, 043108.

32. Chen, G.; Shin, D. H.; Iwasaki, T.; Kawarada, H.; Lee, C. J. Enhanced Field Emission Properties of Vertically Aligned Double-Walled Nanotube Array. *Nanotechnology* **2008**, *19*, 415703.

33. Zhong, G.; Iwasaki, T.; Honda, K.; Furukawa, Y.; Ohdomari, I.; Kawarada, H. Low Temperature Synthesis of Extremely Dense and Vertically Aligned Single-Walled Carbon Nanotubes. *Jpn. J. Appl. Phys.* **2005**, *44*, 1558.

34. Bachilo, S. M.; Strano, M. S.; Kittrell, C.; Hauge, R. H.; Smally, R. E.; Weisman, R. B. Structure-Assigned Optical Spectra of Single-Walled Carbon Nanotubes. *Science* **2002**, *298*, 2361–2366.

35. Brown, S. D. M.; Jorio, A.; Corio, P.; Dresselhaus, M. S.; Dresselhaus, G.; Saito, R.; Kneipp, K. Origin of the Breit−Wigner−Fano Lineshape of the Tangential G-band Feature of Metallic Carbon Nanotubes. *Phys. Rev. B* **2001**, *63*, 155414.

36. Dresselhaus, M. S.; Dresselhaus, G.; Jorio, A. Raman Spectroscopy of Carbon Nanotubes in 1997 and 2007. *J. Phys. Chem. C* **2007**, *111*, 17887–17893.

37. Park, J. S.; Oyama, Y.; Saito, R.; Izumida, W.; Jiang, J.; Sato, K.; Fantini, C.; Jorio, A.; Dresselhaus, G.; Dresselhaus, M. S. Raman Resonance Window of Single-Wall Carbon Nanotubes. *Phys. Rev. B* **2006** *74*, 165414.

38. Collins, P. G.; Arnold, M. S.; Avouris, P. Engineering Carbon Nanotubes and Nanotube Circuits using Electrical Breakdown. *Science* **2001**, *292*, 706–709.